Intrinsic spin Hall effect in topological semimetals with single Dirac nodal ring

Jiali Chen ⬤, Run-Wu Zhang, Zhi-Ming Yu ⬤, Wei Jiang ⬤,* and Yugui Yao†

Centre for Quantum Physics, Key Laboratory of Advanced Optoelectronic Quantum Architecture and Measurement (MOE),
School of Physics, Beijing Institute of Technology, Beijing 100081, China
and Beijing Key Lab of Nanophotonics & Ultrafine Optoelectronic Systems, School of Physics,
Beijing Institute of Technology, Beijing 100081, China

The spin Hall effect (SHE) maintains a distinct, pivotal role within spintronics. In this study, we systematically investigate the intrinsic SHE of topological semimetals with a single Dirac nodal ring (DNR) in the half-Heusler ABC family of compounds (HfCoAs, HfCoP, HfNiAs, ZrCoP, TaCoGe, TiSiNi, NbCoSi). Taking HfCoAs as an example, we show that an ideal single DNR lies within the $\mathcal{M}_y$ mirror plane adjacent to the Fermi surface when spin-orbit coupling (SOC) is absent, as protected by combined space-time inversion ($\mathcal{PT}$) symmetry and $\mathcal{M}_y$ mirror-reflection symmetry. With the inclusion of the SOC, the DNR is gapped out resulting in plenty of minimal band gap near the Fermi level, which yields a large spin Hall conductivity owing to the large spin Berry curvature hotspots around the nodal ring. Our research provides a comprehensive understanding of spin transport properties inherent in the simplest topological DNR semimetals, providing a solid foundation for exploring and engineering more complicated nodal line semimetals. This work may also offer practical applications in advancing spintronics device development with suitable SHE materials.

I. INTRODUCTION

In recent years, the rapid advancement of electronic devices has been driven by continuous miniaturization. However, there exists a fundamental limit to this process as the size of electronic components approaches the atomic scale, which is limited by the quantum size effect [1,2]. To overcome this threshold, researchers have been exploring new approaches to electronic devices, such as spintronics, which use the spin of electrons as an information carrier instead of the electronic charge employed in traditional electronics (e.g., CMOS devices) [3–6]. One important ingredient of spintronics is the use of the spin Hall effect (SHE) [7,8] to enable electrons with different spin directions to move and accumulate in a predetermined direction, obviating the necessity for an external magnetic field [9]. This creates opportunities for spin manipulation in nonmagnetic materials.

Topological semimetals (TSM) [10–14] have attracted significant attention due to their unique electronic properties. Since the intrinsic spin Hall conductivity (SHC) is intimately related to the spin Berry curvature of the electronic bands and SOC [7,9,15], these materials show an enhanced intrinsic SHC around the nontrivial band crossings near the Fermi surface along with nontrivial Berry phases [16]. Simultaneously, their minimal density of states near the Fermi surface results in a correspondingly small longitudinal charge conductivity. Consequently, the spin Hall angle (SHA) [17], delineated as the ratio of the SHC to the charge conductivity, could surpass that of topological metals [18]. These properties make topological semimetals promising candidates for spintronics applications.

Topological semimetals can be classified based on the dimension of their band crossing, extending from zero-dimensional nodal points [19–24], one-dimensional nodal lines/rings [25–31], to two-dimensional nodal surface semimetals [32–34]. Compared to the case of isolated nodal points, a nodal line/ring or nodal surface comprising a continuous assembly of nodal points in the Brillouin zone (BZ) could significantly enhance the SHE, given their increased number of band anticrossing points [35]. Nevertheless, those systems usually host complex electronic structures with mixed nodal and bulk states, adding difficulties in distinguishing the pure contribution from the nodal states and unraveling the underlying mechanism for the enhancement of SHE. Considering these factors, topological semimetals with a single Dirac nodal ring (DNR) may serve as an ideal starting point for studying the fundamentals of intrinsic SHE and exploring their potential SHE enhancement mechanisms.

In this study, based on *ab initio* calculations and symmetry analysis, we propose a family of topological DNR semimetals in the half-Heusler (ABC) compounds when the SOC is ignored. The representative material HfCoAs shows a distinguished clean single nodal ring near the Fermi level, a feature uncommonly observed among topological nodal line semimetals. Further, we undertake a comprehensive examination of the topological properties and the intrinsic SHC within the material HfCoAs in the presence of SOC. The DNR is fully gapped with plenty of minimal band gap, and spin Berry curvature is large along the gapped nodal ring, which results in a considerable SHC in the system. Additionally, we examine

---

*wjiang@bit.edu.cn
†ygyao@bit.edu.cn

the family of half-Heusler ABC compounds (HfCoAs, Hf-CoP, HfNiAs, ZrCoP, TaCoGe, TiSiNi, NbCoSi), which show similar band structures that serve as promising SHE materials. Our work reveals a promising platform for studying the interplay between SHE and the topological band crossings in nodal line systems. It is worth noting that the HfCoAs family of materials have been synthesized experimentally [36], which lays the crucial foundation for their practical application in spintronics, for example, as magnetic switching materials.

II. METHOD

To investigate the electronic band structure, topological properties, and intrinsic SHE, we have performed first-principles calculations based on the density functional theory (DFT). All first-principles calculations were conducted employing the Vienna *ab initio* simulation package (VASP) [37,38], which is treated by the projector augmented wave (PAW) [39] method and utilizes a plane wave basis set. The exchange and correlation terms were considered at the level of generalized gradient approximation (GGA) [39] within the scheme of the Perdew-Burke-Ernzerhof (PBE) [40] functional. The plane-wave cutoff energy is chosen as 500 eV, accompanied by an $8 \times 13 \times 7$ k-point grid used for self-consistent calculations. The topological properties associated with HfCoAs system, including topological number Z_2 [25,28,29,41,42], the evolution of Wilson loop [43], surface states [25], Berry phase [43], and so on, are investigated by constructing the maximally localized Wannier functions with Wannier90 [44,45] and WannierTools [46]. For symmetry analysis, we also utilize the Irvsp package [47] to get the irreducible representation of the energy band.

By calculating and analyzing the fatband structure (SM [48]) [49], the Bloch states of low energy spectrum can be projected into highly symmetric atomic orbitals like Wannier functions (specifically, Hf-d, Co-d, and As-p orbitals). The tight-binding Hamiltonian is constructed and used to compute the SHC, which is based on the linear-response Kubo formula approach [50,51]. Note that we implemented this scheme in a module of the Wannier90 package [44,45,52]. To include SOC in our analysis, we introduce an additional term $\mathcal{H}_{SOC}^{\alpha\beta} \propto \sigma \cdot L$ to the Hamiltonian, effectively coupling the spin with the angular momentum. This addition, as implemented in the VASP package, is pivotal for accurately computing the SHC [53]. The SHC, $\sigma_{\alpha\beta}^{\text{spin}\,\gamma}$, can be mathematically expressed as

$$\sigma_{\alpha\beta}^{\text{spin}\,\gamma}(\omega) = \frac{e}{2} \frac{1}{V N_k} \sum_k \Omega_{\alpha\beta}^{\text{spin}\,\gamma}(\boldsymbol{k}), \quad (1)$$

where V is the cell volume, and N_k represents the number of k points used for sampling the Brillouin zone. Analogous to the ordinary Berry curvature, $\Omega_{\alpha\beta}^{\text{spin}\,\gamma}(\boldsymbol{k})$ is a k-resolved spin Berry curvature term, which sums over occupied bands [54]:

$$\Omega_{\alpha\beta}^{\text{spin}\,\gamma}(\boldsymbol{k}) = \sum_n f_{n\boldsymbol{k}} \Omega_{n,\alpha\beta}^{\text{spin}\,\gamma}(\boldsymbol{k}), \quad (2)$$

where $f_{n\vec{k}} = f(\varepsilon_{n\vec{k}})$ is the Fermi-Dirac distribution for the nth band, and $\Omega_{n,\alpha\beta}^{\text{spin}\,\gamma}(\boldsymbol{k})$ is the band-projected spin Berry curvature term:

$$\Omega_{n,\alpha\beta}^{\text{spin}\,\gamma}(\boldsymbol{k}) = \hbar^2 \sum_{m \neq n} \frac{-2\,\text{Im}\left[\langle n\boldsymbol{k}| \frac{1}{2}\{\hat{\sigma}_\gamma, \hat{v}_\alpha\} |m\boldsymbol{k}\rangle \langle m\boldsymbol{k}|\hat{v}_\beta|n\boldsymbol{k}\rangle \right]}{(\epsilon_{n\boldsymbol{k}} - \epsilon_{m\boldsymbol{k}})^2 - (\hbar\omega + i\eta)^2}. \quad (3)$$

The unit of the $\Omega_{n,\alpha\beta}^{\text{spin}\,\gamma}(\boldsymbol{k})$ and $\sigma_{\alpha\beta}^{\text{spin}\,\gamma}$ are denoted in Å^2 and $(\hbar/e)$S/cm, respectively. The spin current operator is represented by $\hat{\jmath}_\alpha^{s,\gamma} = \frac{1}{2}\{\hat{v}_\alpha, \hat{s}_\gamma\}$ with the spin operator $\hat{s}_\gamma = \frac{\hbar}{2}\hat{\sigma}_\gamma$, which flows along the α direction with the spin polarization along γ, generated by an electric field E_β along the β direction, i.e., $j_\alpha^{s,\gamma} = \sigma_{\alpha\beta}^\gamma E_\beta$. The velocity operator is given by $v_\beta = \frac{1}{\hbar} \frac{\partial H}{\partial k_\beta}$, where $\alpha, \beta, \gamma = x, y, z$ are Cartesian components. $|n\boldsymbol{k}\rangle$ is the eigenvector for the Hamiltonian H at the eigenvalue $E_{n\boldsymbol{k}}$. In the following section, we will focus on the direct current (dc) spin Hall conductivity, which means $\omega = 0$.

For the computation of intrinsic SHC, we employed a Brillouin Zone summation on a $70 \times 70 \times 70$ k grid and set adapted k mesh equal to seven (convergence test in the SM [48]), a procedure intended to deal with the dramatic variation in the spin Berry curvature. It is worth noting that the spin matrix file, *.spn* file, required for the Wannier90 SHC calculation was generated using the WannierBerri package in our work [55,56].

III. SINGLE DIRAC NODAL RING

It has been known that in the absence of SOC or when the SOC is negligible, the 3D nodal line could exist if the system has $\mathcal{PT}$ symmetry, and further, if the system also has mirror symmetry, the position of the nodal lines will be constrained accordingly [29,41]. To study the system with a single nodal ring, we focus on material systems that have $\mathcal{PT}$ symmetry, also with one mirror symmetry, i.e., the half-Heusler ABC compounds, which share the orthorhombic lattice structure with space group Pnma/mmm (No. 62). The primitive unit cell and front views of the conventional cell of the representative HfCoAs are illustrated in Figs. 1(a) and 1(b), respectively. In Fig. 1(b), it is clear that the system contains one mirror plane $\mathcal{M}_y$. Through DFT calculations, the compound is found to be a nonmagnetic system. Moreover, we should note the HfCoAs system contains d-orbital electrons, which are known for underestimated electronic correlation effects in the conventional exchange-correlation functionals, like the generalized gradient approximation (GGA). To account for potential errors in exchange correlation, the Hubbard term with the on-site Coulombic (U) and exchange (J) terms are usually applied [57].

However, upon testing the impact of varying U values in our system, we found that the influence on the overall system was relatively minimal. Notably, at $U = 0$, the lattice constants obtained from the structural relaxation of the system aligned more closely with the experimental values. Therefore, we choose $U = 0$ for the subsequent calculations; see more calculation details in the SM [48].

We further calculated the electronic band structures and density of states (DOS) of HfCoAs, as shown in Fig. 1(c). Note that the Fermi energy is set to zero for reference. On the left panel, the solid lines represent the DFT calculated band structure, in which dark and green lines denote the bands without and with spin-orbit coupling (SOC), respectively. In the absence of SOC, the emergence of band crossing points is apparent at $\Gamma - X$ and $\Gamma - Z$ [insets in Fig. 1(c)], which are labeled as $\mathcal{D}_1$ and $\mathcal{D}_2$, respectively. To further check the existence of other potential crossing points, we perform a
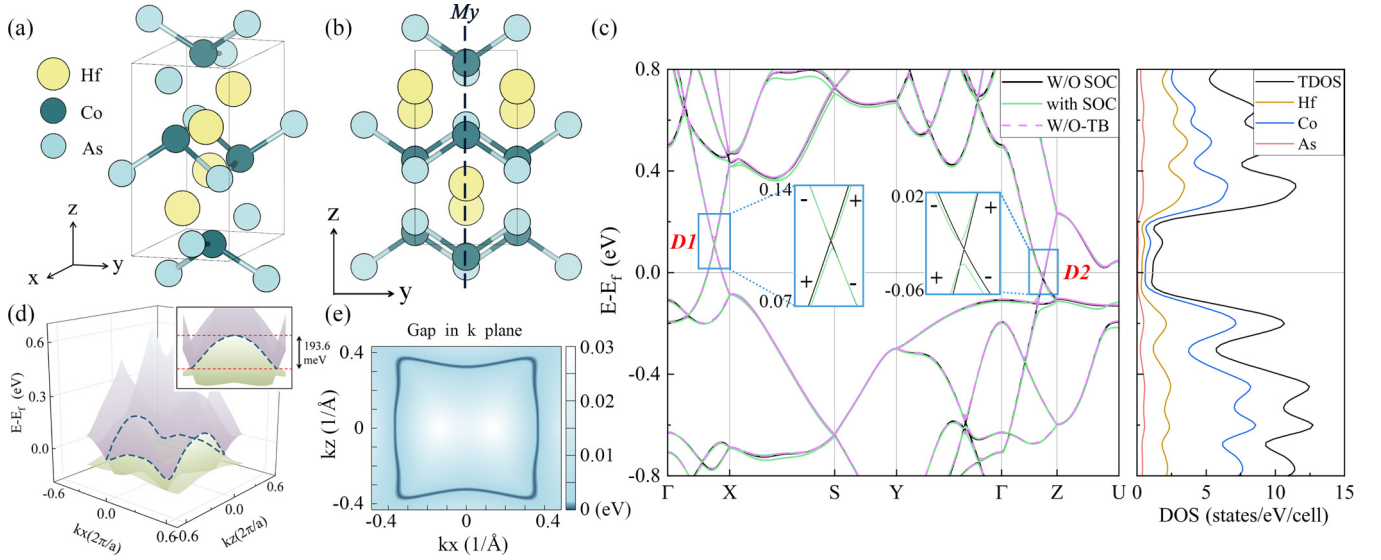
FIG. 1. (a) The orthorhombic primitive unit cell of HfCoAs. Hf, Co, and As atoms are colored yellow, dark green, and light green, respectively. (b) The front view of the conventional cell of HfCoAs and the $\mathcal{M}_y$ symmetry can be seen (dotted line). The black lines indicate the unit cell. (c) Calculated electronic band structure of HfCoAs, without and with SOC, as well as the projected density of states (PDOS). In the absence of SOC (solid black lines), Dirac crossings are visible along $\Gamma - X$ and $\Gamma - Z$, which become fully gapped in the presence of SOC (solid green lines) as shown in the insets. The wannier-interpolated band structure is indicated by dotted pink lines. (d) The three-dimensional (3D) band structures of HfCoAs without SOC. The topological nodal ring on the kx-kz plane is highlighted by dotted blue lines and the dispersion range of the nodal ring is $\Delta E = 193.6$ meV, which is shown as insets. (e) Illustration of the nodal rings in the $ky = 0$ plane shows the full loop.

careful calculation of the 3D band structure and the energy gap between the two bands near the Fermi level: gap $(k) = E_{\text{Upper-fermi}}(k) - E_{\text{Lower-fermi}}(k)$. It is found that crossing points actually persist along all directions around the Γ point in the $ky = 0$ plane, resulting in a single nodal ring, as indicated by dotted blue lines in Figs. 1(d) and 1(e). Note that the nodal ring has an energt range $(-84.4, 109.2)$ meV with an energy dispersion, ΔE, about 193.6 meV, as illustrated in the inset of Fig. 1(d). Since both time-reversal and inversion symmetries are present, each band is doubly degenerate. Therefore, the nodal ring is fourfold degenerate, resulting in a Dirac nodal ring semimetal.

While SOC is included, the fourfold degenerate DNR becomes fully gapped out, resulting in two twofold degenerate states near the Fermi level. The insets of Fig. 1(c) display the small gap regions, with $\Delta E_{\mathcal{D}_1} \approx 19$ meV, $\Delta E_{\mathcal{D}_2} \approx 11$ meV, and the range of gap for all the points on the nodal ring is $4 \sim 88$ meV (SM [48]). This gapping out along a large number of k points plays a central role in producing the large SHC, a topic we shall delve into subsequently. Note that the small DOS [right panel of Fig. 1(c)] near the Fermi level usually suggests a relatively small charge conductivity that could yield a large SHA, which is beneficial for the energetic efficient spintronics applications. To calculate the topological and transport properties, we fitted the DFT calculated bands both with and without SOC using Wannier90 utilizing 104 Wannier orbits (52 for each spin), as shown in Fig. 1(c) with dotted pink lines for the case without SOC. The comparison reveals a perfect match between the DFT calculated and Wannier-represented bands near the Fermi energy ± 2 eV.

IV. TOPOLOGICAL PROPERTY

A system is said to be topologically nontrivial if the filled bands can't be adiabatically deformed into an atomic insulator without closing the gap, meaning that some topological invariants [42,58–60] cannot be changed continuously. Topological invariants can be determined directly from the band structure of the material, using various algorithms like Wilson loop calculations [43], the Berry phase method [61–63], etc. These methods typically require solving the full band structure. On the other hand, the theory of band representations (BR) [64] provides another more general and systematic approach, which is the basis of topological quantum chemistry (TQC) [65–68]. It leverages the symmetry of the crystal and its wave function, which is encoded in the irreducible representation of the high symmetry points (and lines/planes if needed), to identify the topology [67,69–71]. To characterize the topological nature of the HfCoAs system, we utilize both the concept of topological invariants and the BR theory in the following.

From the band structure shown in Fig. 1(c), one observes that when SOC is not considered, there are two nodes located at $\Gamma - X$ and $\Gamma - Z$. Due to the presence of $\mathcal{PT}$ symmetry [72–75] in HfCoAs, the system could host more Dirac nodes beyond the two Dirac nodes $\mathcal{D}_1$ and $\mathcal{D}_2$, forming a nodal ring [41], as we have verified. Note that $\mathcal{PT}$ symmetry is enough to guarantee DNR, and to check this, we calculate the Berry phase [73] for a closed k path in the 3D BZ. For a path not enclosing the nodal ring, the Berry phase is zero, while for a path encircling the nodal ring, the Berry phase is π ($\pm\pi$, with the sign depending on the path direction) [28,29], confirming the topological feature of this DNR.
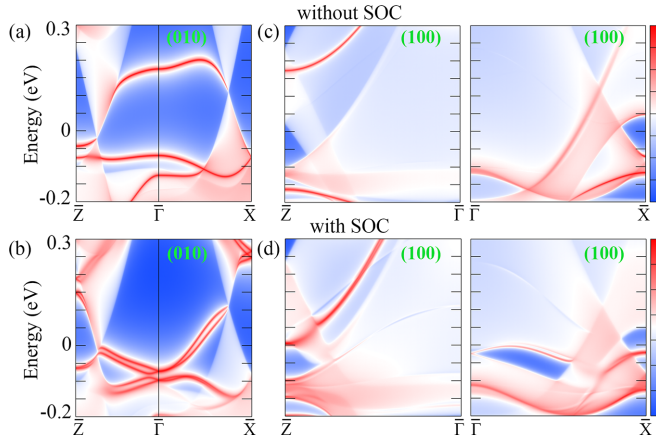
FIG. 2. Surface spectra on (010) surface without (a) and with (b) SOC. The redness of color represents a larger density of the states from the surface. Surface spectra on (100) and (001) surfaces without (c) and with (d) SOC.

In addition, we found that the DNR is located in the mirror-invariant $k_y = 0$ plane, which is actually induced by the extra $\mathcal{M}_y$ mirror symmetry of the half-Heusler compounds [76,77]. To further evaluate the topological feature of this $\mathcal{M}_y$ mirror symmetry, we compute the irreducible representations of the energy bands along high-symmetry paths: $\Gamma - X - S - Y - \Gamma - Z - U$. Taking point $\mathcal{D}_1$ as an example, at the Γ point, the two states near the Fermi level belong to irreducible representation GM3+ and GM1+, corresponding to -1 and $+1$ $\mathcal{M}_y$ mirror eigenvalues. While at the Z point, the $\mathcal{M}_y$ mirror eigenvalues of the two states near the Fermi level, which belong to irreducible representation Z1 and Z2, are $+2$ and -2. As a result, the compatibility relation [67] is not satisfied on the high-symmetry line connecting the points Γ and Z. Consequently, an obligatory energy band crossing between the conduction band and the valence band is necessitated. Similarly, we extend this analysis to the $\Gamma - X$ path, which confirms the occurrence of band inversion. Since the two crossing bands have different mirror eigenvalues, we could indeed confirm that the DNR is topological and protected by the $\mathcal{M}_y$ mirror symmetry.

Furthermore, the band inversions at the Dirac nodes $\mathcal{D}_1$ and $\mathcal{D}_2$ suggest the existence of topological nontrivial surface state [20,22,30,78]. Therefore, we calculate the surface state of HfCoAs (010) surface without and with the SOC, as shown in Figs. 2(a) and 2(b), respectively. We notice that some Fermi arc states connecting the Dirac nodes are observed in the DNR semimetal phase of HfCoAs when the SOC is neglected [Fig. 2(a)]. When the SOC is included, topological protected surface states appear on the $Z - \Gamma$ and $\Gamma - X$ paths being clearly visible [Fig. 2(b)] due to the spin splits and the gap opening of the node line, revealing the transition from a topological semimetal to a 3D small-gap topological insulator (TI). The gapped system is further confirmed to be topologically nontrivial with Z_2 indices (1;000) [42], which is obtained by examining the evolution of the Wannier charge center across six time-reversal invariant planes in the Brillouin zone (more details can be found in the SM [48]). In addition, there is another approach to compute the Z_2 topological invariant by

computing the lattice Chern number for half of the Brillouin zone [79,80]. Both methods offer insights into the topological properties of materials through different computational frameworks. We note that the DNR is fully gapped while considering SOC in the HfCoAs system, which, however, is not an ideal topological insulator but a compensated semimetal because of the crossing bands at the Fermi level.

V. INTRINSIC SPIN HALL EFFECT

Induced by spin-orbit coupling, the gap opening near the band anticrossing points can contribute strong spin Berry curvature (SBC) in analogy to the ordinary Berry curvature [9], meanwhile, the small energy denominator in the Kubo expression contributes to an augmented SHC significantly [50,51]. To maximize the SHC, it is essential to increase the number of band anticrossing points, i.e., hotspots, which can be potentially achieved in topological Dirac nodal line or nodal surface systems. The Dirac nodal line semimetal studied here, i.e., HfCoAs, hosts an ideal single topological DNR, which incurs a gap along the DNR when SOC is introduced and may lead to a large SHC. To calculate the intrinsic SHE, we constructed the tight-binding (TB) model Hamiltonian including SOC, and computed the intrinsic SHC through the Kubo formula approach following Eq. (1) [52,81].

The SHC tensor, σ_{ij}^k, is a second-order tensor with 27 elements. Symmetry not only restricts certain elements to be zero but also imposes conditions on the independence of the remaining nonzero elements [82]. In the HfCoAs system, there are six nonzero and independent elements of the SHC tensor, where all three directions of spin flow, charge flow, and spin polarization are mutually perpendicular, i.e., σ_{xy}^z, σ_{yx}^z, σ_{zx}^y, σ_{zy}^x, σ_{yz}^x, and σ_{xz}^y. We note that the integrity of the symmetry within the TB model Hamiltonian is essential to determine the SHC accurately. To verify the accuracy of the fitted Wannier function for the HfCoAs system, we first calculate elements that symmetry requirements dictate to be zero [82,83], and we present these elements in Fig. S9 of the Supplemental Material [48]. The results show that except for some negligible numerical errors, the SHC is indeed close to zero, which indicates that the Hamiltonian we constructed has the necessary symmetries, especially the $\mathcal{M}_y$ mirror symmetry. This confirms that the Wannier90 fitted TB model Hamiltonian is correctly applied.

Further, we determine the values of the six nonzero SHC tensors at the Fermi energy, $\sigma_{xy}^z \approx 97.25$, $\sigma_{yx}^z \approx -102.05$, $\sigma_{zx}^y \approx 74.84$, $\sigma_{zy}^x \approx -218.16$, $\sigma_{yz}^x \approx 238.97$, and $\sigma_{xz}^y \approx -42.36$ ($\hbar/e$)S/cm (shown in the SM [48]), which shows sizable values and is comparable to other semimetals [35,84–86]. Notably, these six elements differ from each other, reflecting the anisotropy of the crystal structure. The accuracy of the calculated SHC was double checked by the symmetry analysis, ensuring the validity of our findings. To better understand the interplay between the DNR and the large SHC, we presented the energy-dependent SHC of the usually studied σ_{xy}^z and a relatively larger σ_{zy}^x component. First, we can clearly see an obvious SHC peak near the Fermi level, e.g., P_1 and P_2 for σ_{xy}^z and σ_{zy}^x in Figs. 3(a) and 3(d), respectively, which locates within the energy range of the DNR $(-84.4, 109.2)$ meV (highlighted by dashed gray lines).
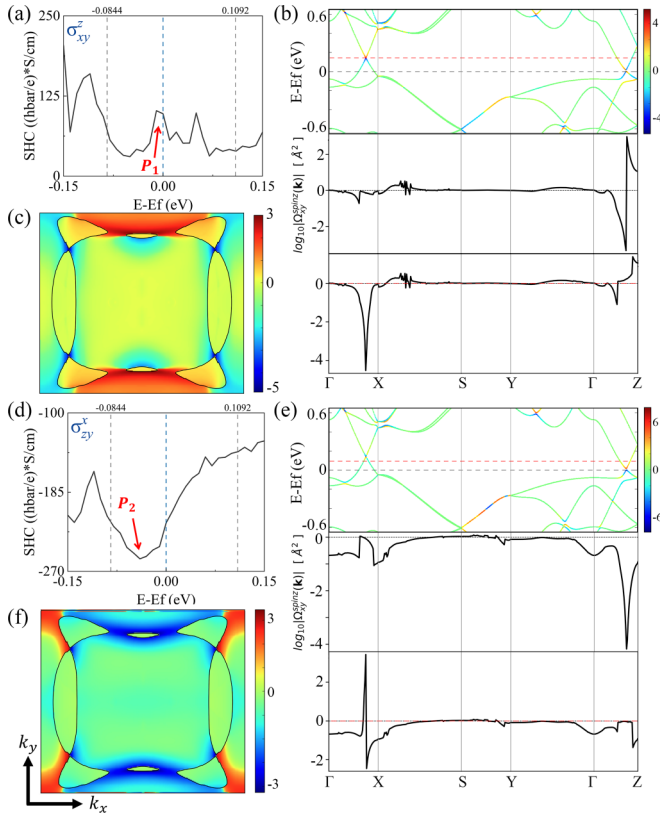
FIG. 3. (a) Calculated intrinsic conventional SHC σ_{xy}^z is in in units of $(\hbar/e)$S/cm. (b) Top panel: Band structure along symmetry lines $\Gamma - X - S - Y - \Gamma - Z$, colored by the band-projected Berry curvaturelike term $\Omega_{n,xy}^{\text{spin}\,z}(\boldsymbol{k})$. Bottom panel: k-resolved Berry curvaturelike term $\Omega_{xy}^{\text{spin}\,z}(\boldsymbol{k})$ along the same path in the BZ, note the log scale on the vertical axis. (c) The k-resolved term $\Omega_{xy}^{\text{spin}\,z}(\boldsymbol{k})$ inside the (010) mirror plane. The blue and red colors show the dominant contributions from the gaped-out nodal ring in units of Å^2. Intersections of the Fermi surface with this plane are shown as black lines. (d), (e), (f) Analogous to (a), (b), (c), but for the case of component σ_{zy}^x.

Considering only DNR exists at that energy range that could be the spin Berry curvature (SBC) resources, it suggests the SBC contribution from the DNR to the overall SHC (more details can be found in the SM [48]).

To further verify the DNR enhancement of SHC, we have further calculated and analyzed the k-resolved spin Berry curvature distribution along both the high-symmetry k path and k plane that host the DNR, as well as the energy-resolved spin Berry curvature distribution for the whole band along the high-symmetry k path. Take σ_{xy}^z as an example: by using Wannier interpolation [52,81], we calculate the band structure, colored by the band-projected spin Berry curvature results [upper panel of Fig. 3(b)], $\Omega_{n,xy}^{\text{spin}\,z}(\boldsymbol{k})$ [see Eq. (3)], and the energy-resolved spin Berry curvature distribution [lower panel of Fig. 3(b)] $\Omega_{xy}^{\text{spin}\,z}(\boldsymbol{k})$ [see Eq. (2)] along the path $\Gamma - X - S - Y - \Gamma - Z$ in the BZ. The results shown in Fig. 3(b) show a noticeable contribution of spin Berry curvature (hotspots colored in red and blue) around the DNR with negligible spin Berry curvature from the other bands (colored in green). Similarly, the k-resolved spin Berry curvature plot (lower panel) for the Fermi-energy on points $\mathcal{D}_1$ (red dashed line) or $\mathcal{D}_2$ (dark gray dashed line) reveals large spikes at $\mathcal{D}_1$ or $\mathcal{D}_2$ points. We note that there are certain abnormal spin Berry curvature fluctuations along S–X and S–Y k paths, which are mostly numerical errors that have negligible influence on the SHC results, as supported by the calculation results from different SHC elements (see the SM for more details [48]).

To gain a better understanding of the entire gapped-out DNR contribution to the SHC, which is obtained by calculating the spin Berry curvature term at each k point, we plot a heatmap of $\Omega_{xy}^{\text{spin}\,z}(\boldsymbol{k})$ in the $ky = 0$ mirror plane, as shown in Fig. 3(c). Intersections of the Fermi surface with the (010) plane are denoted by the dark line that also corresponds to the distribution of the DNR. The results show clearly that the largest absolute values (colored in red and blue), e.g., large spin Berry curvature, are located around the DNR, further validating the DNR contribution to the SHC. We also calculate and compare the differences between different SHC components, especially the one (σ_{zy}^x) with a relatively large SHC, as shown in Fig. 3(d). The band and band-projected characteristics are shown in Fig. 3(e), bearing a similarity to σ_{xy}^z. In Fig. 3(f), we also calculated the $\Omega_{zy}^{\text{spin}\,x}(\boldsymbol{k})$, consistent with the discussions of Fig. 3(c) and the SHC is mainly contributed from the nodal ring. However, in this case, there are more blue contributions than red, which leads to the negative σ_{zy}^x with positive σ_{xy}^z values.

In fact, the enhanced SHC near the Fermi level is not only due to the large spin Berry curvature along the nodal ring, but also highly related to stationary points in the energy dispersion of the nodal ring [87,88]. So we also calculated the energy dispersion and DOS from the nodal rings eigenvalues and found sharp peaks (van Hove singularities) in the DOS, which is consistent with the peaks of the SHC results. This better demonstrates the connection between the DNR and enhanced SHC (more details can be found in the SM [48].)

VI. PROMISING MATERIAL CANDIDATES

The family of half-Heusler semimetal ABC (HfCoAs, HfCoP, HfNiAs, ZrCoP, TaCoGe, TiSiNi, NbCoSi) share the same orthorhombic lattice structure with the space group of Pnma/mmm (No. 62). These compounds were extracted from the ICSD database provided by the material project [89]. To be noted, all the ABC compounds studied in this work are realistic materials that have been synthesized in experiments [36,90–94]. Using HfCoAs as a representative example, we have proved that this is a promising material candidate that can provide large SHC due to the presence of a small gap in the nodal ring. As shown in Fig. 4, based on *ab initio* calculations, we further calculate the band structure of the other materials (TaCoGe, TiSiNi, ZrCoP, HfCoP, NbCoSi, HfNiAs) in the same family without and with SOC. We notice that the essential features, including the nodal ring and small band gap induced by SOC, are also shared by other members of this material family. Due to these favorable properties, we expect that other compounds in this family also possess large intrinsic SHE, which is a fascinating property for the development of future spintronic devices.
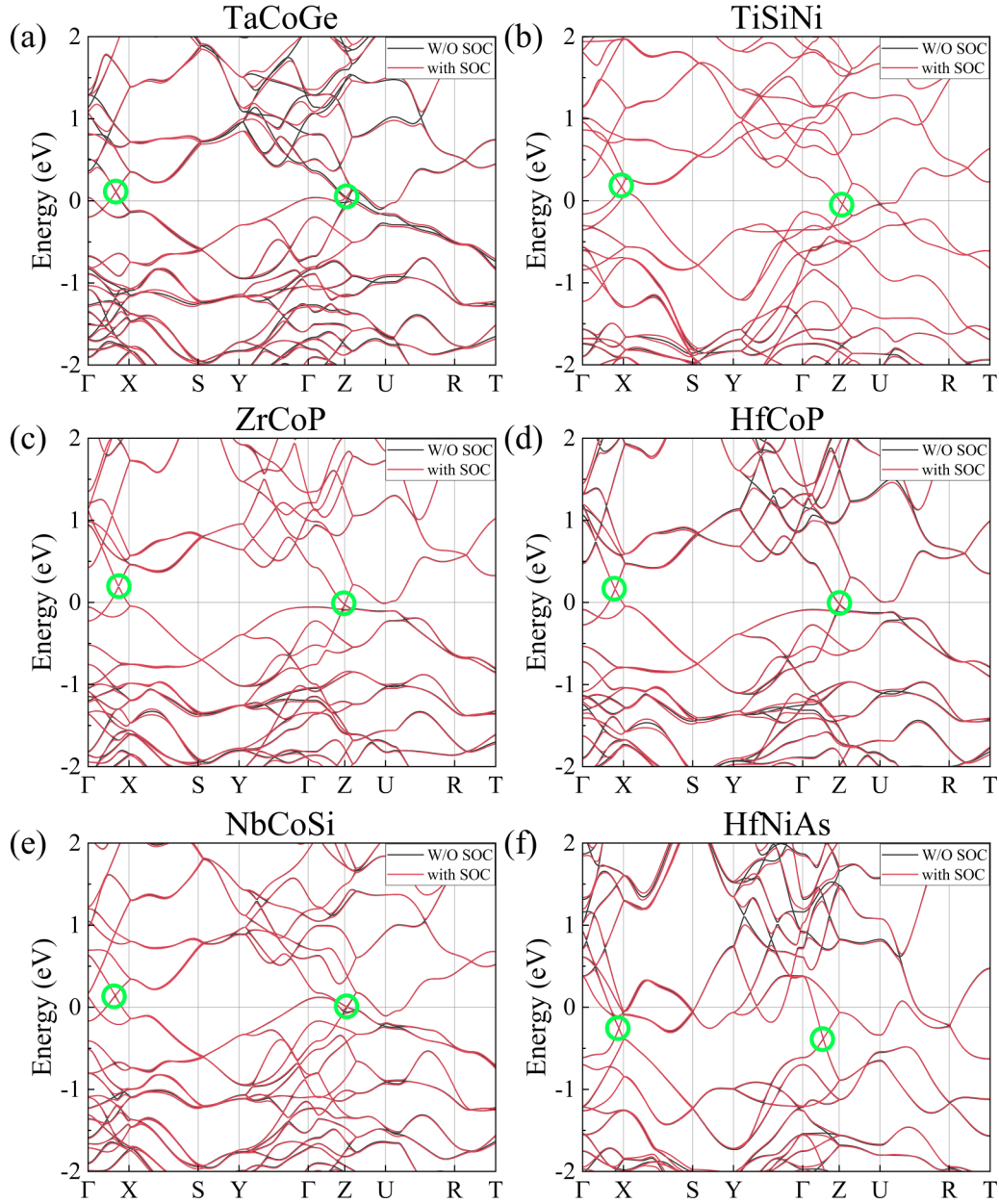
FIG. 4. (a)–(f) Electronic band structure of half-Heusler materials (TaCoGe, TiSiNi, ZrCoP, HfCoP, NbCoSi, HfNiAs), while without SOC (Solid black lines) and with SOC (Solid red lines) are presented in dark and red. The band crossings that constitute the DNR are highlighted by green circles.

VII. CONCLUSION

In conclusion, our analysis establishes that HfCoAs, an experimentally synthesized compound, behaves as a topological Dirac nodal ring (DNR) semimetal when spin-orbit coupling (SOC) is disregarded. This DNR is maintained by both $\mathcal{PT}$ and $\mathcal{M}_y$ symmetries. The inclusion of SOC results in a small gap along the original DNR near the Fermi energy, and because of the small energy difference, spin Berry curvature is large there, leading to a large SHC. Moreover, compared to pure metals, these topological semimetals are anticipated to exhibit significantly reduced charge conductivity, leading to a larger spin Hall angle. The insight gathered from this study bolsters our understanding of the fundamental characteristics of DNR's contribution to SHC in HfCoAs, marking a crucial step toward the development of future spintronic devices.

[1] K. Elphick, W. Frost, M. Samiepour, T. Kubota, K. Takanashi, H. Sukegawa, S. Mitani, and A. Hirohata, Heusler alloys for spintronic devices: Review on recent development and future perspectives, Sci. Technol. Adv. Mater. **22**, 235 (2021).

[2] A. Hirohata, K. Yamada, Y. Nakatani, I.-L. Prejbeanu, B. Diény, P. Pirro, and B. Hillebrands, Review on spintronics: Principles and device applications, J. Magn. Magn. Mater. **509**, 166711 (2020).

[3] Y. Zhang, H. Y. Yuan, X. S. Wang, and X. R. Wang, Breaking the current density threshold in spin-orbit-torque magnetic random access memory, Phys. Rev. B **97**, 144416 (2018).

[4] S. Shi, Y. Ou, S. V. Aradhya, D. C. Ralph, and R. A. Buhrman, Fast low-current spin-orbit-torque switching of magnetic tunnel junctions through atomic modifications of the free-layer interfaces, Phys. Rev. Appl. **9**, 011002(R) (2018).

[5] S.-h. C. Baek, V. P. Amin, Y.-W. Oh, G. Go, S.-J. Lee, G.-H. Lee, K.-J. Kim, M. D. Stiles, B.-G. Park, and K.-J. Lee, Spin currents and spin–orbit torques in ferromagnetic trilayers, Nat. Mater. **17**, 509 (2018).

[6] A. Manchon and S. Zhang, Theory of spin torque due to spin-orbit coupling, Phys. Rev. B **79**, 094422 (2009).

[7] J. Sinova, D. Culcer, Q. Niu, N. A. Sinitsyn, T. Jungwirth, and A. H. MacDonald, Universal intrinsic spin Hall effect, Phys. Rev. Lett. **92**, 126603 (2004).

[8] S. Murakami, N. Nagosa, and S.-C. Zhang, SU(2) non-Abelian holonomy and dissipationless spin current in semiconductors, Phys. Rev. B **69**, 235206 (2004).

[9] J. Sinova, S. O. Valenzuela, J. Wunderlich, C. H. Back, and T. Jungwirth, Spin Hall effects, Rev. Mod. Phys. **87**, 1213 (2015).

[10] C.-K. Chiu, J. C. Y. Teo, A. P. Schnyder, and S. Ryu, Classification of topological quantum matter with symmetries, Rev. Mod. Phys. **88**, 035005 (2016).

[11] A. Bansil, H. Lin, and T. Das, *Colloquium*: Topological band theory, Rev. Mod. Phys. **88**, 021004 (2016).

[12] N. P. Armitage, E. J. Mele, and A. Vishwanath, Weyl and Dirac semimetals in three-dimensional solids, Rev. Mod. Phys. **90**, 015001 (2018).

[13] W. Jiang, H. Huang, F. Liu, J.-P. Wang, and T. Low, Magnetic weyl semimetals with diamond structure realized in spinel compounds, Phys. Rev. B **101**, 121113(R) (2020).

[14] W. Jiang, D. J. P. de Sousa, J.-P. Wang, and T. Low, Giant anomalous Hall effect due to double-degenerate quasiflat bands, Phys. Rev. Lett. **126**, 106601 (2021).

[15] S. Murakami, N. Nagaosa, and S.-C. Zhang, Spin-hall insulator, Phys. Rev. Lett. **93**, 156804 (2004).

[16] B.-J. Yang and N. Nagaosa, Classification of stable three-dimensional Dirac semimetals with nontrivial topology, Nat. Commun. **5**, 4898 (2014).

[17] W. Zhang, W. Han, S.-H. Yang, Y. Sun, Y. Zhang, B. Yan, and S. S. P. Parkin, Giant facet-dependent spin-orbit torque and spin Hall conductivity in the triangular antiferromagnet IrMn₃, Sci. Adv. **2**, e1600759 (2016).

[18] A. Hoffmann, Spin Hall effects in metals, IEEE Trans. Magn. **49**, 5172 (2013).

[19] G. Xu, H. Weng, Z. Wang, X. Dai, and Z. Fang, Chern semimetal and the quantized anomalous Hall effect in HgCr 2 Se 4, Phys. Rev. Lett. **107**, 186806 (2011).

[20] X. Wan, A. M. Turner, A. Vishwanath, and S. Y. Savrasov, Topological semimetal and Fermi-arc surface states in the elec-

[21] tronic structure of pyrochlore iridates, Phys. Rev. B **83**, 205101 (2011).

[21] H. Weng, C. Fang, Z. Fang, B. A. Bernevig, and X. Dai, Weyl semimetal phase in noncentrosymmetric transition-metal monophosphides, Phys. Rev. X **5**, 011029 (2015).

[22] Z. Wang, Y. Sun, X.-Q. Chen, C. Franchini, G. Xu, H. Weng, X. Dai, and Z. Fang, Dirac semimetal and topological phase transitions in A₃Bi (A = Na, K, Rb), Phys. Rev. B **85**, 195320 (2012).

[23] Z. Wang, H. Weng, Q. Wu, X. Dai, and Z. Fang, Three-dimensional Dirac semimetal and quantum transport in Cd₃As₂, Phys. Rev. B **88**, 125427 (2013).

[24] X.-L. Sheng, Z. Wang, R. Yu, H. Weng, Z. Fang, and X. Dai, Topological insulator to Dirac semimetal transition driven by sign change of spin-orbit coupling in thallium nitride, Phys. Rev. B **90**, 245308 (2014).

[25] C.-K. Chiu and A. P. Schnyder, Classification of reflection-symmetry-protected topological semimetals and nodal superconductors, Phys. Rev. B **90**, 205136 (2014).

[26] R. Takahashi, M. Hirayama, and S. Murakami, Spinless hourglass nodal-line semimetals, Phys. Rev. B **96**, 155206 (2017).

[27] S.-Y. Yang, H. Yang, E. Derunova, S. S. P. Parkin, B. Yan, and M. N. Ali, Symmetry demanded topological nodal-line materials, Adv. Phys.: X **3**, 1414631 (2018).

[28] C. Fang, H. Weng, X. Dai, and Z. Fang, Topological nodal line semimetals, Chin. Phys. B **25**, 117106 (2016).

[29] C. Fang, Y. Chen, H.-Y. Kee, and L. Fu, Topological nodal line semimetals with and without spin-orbital coupling, Phys. Rev. B **92**, 081201(R) (2015).

[30] A. A. Burkov, M. D. Hook, and L. Balents, Topological nodal semimetals, Phys. Rev. B **84**, 235126 (2011).

[31] R. Yu, H. Weng, Z. Fang, X. Dai, and X. Hu, Topological node-line semimetal and Dirac semimetal state in antiperovskite Cu₃PdN, Phys. Rev. Lett. **115**, 036807 (2015).

[32] W. Wu, Y. Liu, S. Li, C. Zhong, Z.-M. Yu, X.-L. Sheng, Y. X. Zhao, and S. A. Yang, Nodal surface semimetals: Theory and material realization, Phys. Rev. B **97**, 115125 (2018).

[33] Q.-F. Liang, J. Zhou, R. Yu, Z. Wang, and H. Weng, Node-surface and node-line Fermions from nonsymmorphic lattice symmetries, Phys. Rev. B **93**, 085427 (2016).

[34] C. Zhong, Y. Chen, Y. Xie, S. A. Yang, M. L. Cohen, and S. B. Zhang, Towards three-dimensional Weyl-surface semimetals in graphene networks, Nanoscale **8**, 7232 (2016).

[35] Y. Sun, Y. Zhang, C. Felser, and B. Yan, Strong intrinsic spin Hall effect in the TaAs family of Weyl semimetals, Phys. Rev. Lett. **117**, 146403 (2016).

[36] H. Kleinke and H. F. Franzen, Crystal structures, bonding and electronic structures of MM′As, a Series of New Ternary Arsenides (M = Zr, Hf; M′ = Fe, Co, Ni), Z. Anorg. Allg. Chem. **624**, 51 (1998).

[37] G. Kresse and J. Furthmüller, Efficiency of ab-initio total energy calculations for metals and semiconductors using a plane-wave basis set, Comput. Mater. Sci. **6**, 15 (1996).

[38] G. Kresse and J. Hafner, *Ab initio* molecular-dynamics simulation of the liquid-metal–amorphous-semiconductor transition in germanium, Phys. Rev. B **49**, 14251 (1994).

[39] P. E. Blöchl, Projector augmented-wave method, Phys. Rev. B **50**, 17953 (1994).

[40] J. P. Perdew, J. A. Chevary, S. H. Vosko, K. A. Jackson, M. R. Pederson, D. J. Singh, and C. Fiolhais, Atoms, molecules,

solids, and surfaces: Applications of the generalized gradient approximation for exchange and correlation, Phys. Rev. B **46**, 6671 (1992).

[41] H. Weng, Y. Liang, Q. Xu, R. Yu, Z. Fang, X. Dai, and Y. Kawazoe, Topological node-line semimetal in three-dimensional graphene networks, Phys. Rev. B **92**, 045108 (2015).

[42] L. Fu, C. L. Kane, and E. J. Mele, Topological insulators in three dimensions, Phys. Rev. Lett. **98**, 106803 (2007).

[43] J. K. Asbóth, L. Oroszlány, and A. Pályi, A short course on topological insulators: Band-structure topology and edge states in one and two dimensions, arXiv:1509.02295.

[44] N. Marzari and D. Vanderbilt, Maximally localized generalized wannier functions for composite energy bands, Phys. Rev. B **56**, 12847 (1997).

[45] I. Souza, N. Marzari, and D. Vanderbilt, Maximally localized wannier functions for entangled energy bands, Phys. Rev. B **65**, 035109 (2001).

[46] Q. Wu, S. Zhang, H.-F. Song, M. Troyer, and A. A. Soluyanov, WannierTools: An open-source software package for novel topological materials, Comput. Phys. Commun. **224**, 405 (2018).

[47] J. Gao, Q. Wu, C. Persson, and Z. Wang, Irvsp: To obtain irreducible representations of electronic states in the VASP, Comput. Phys. Commun. **261**, 107760 (2021).

[48] See Supplemental Material at http://link.aps.org/supplemental/10.1103/PhysRevMaterials.8.044201 for intrinsic spin Hall effect in Dirac nodal line semimetals with DFT $+ U$ calculations, brillouin zone with high symmetry k points, topological characteristics, topological nodal lines, and SHC calculations,

[49] V. Wang, N. Xu, J.-C. Liu, G. Tang, and W.-T. Geng, VASPKIT: A user-friendly interface facilitating high-throughput computing and analysis using VASP code, Comput. Phys. Commun. **267**, 108033 (2021).

[50] G. Y. Guo, Y. Yao, and Q. Niu, *Ab initio* calculation of the intrinsic spin Hall effect in semiconductors, Phys. Rev. Lett. **94**, 226601 (2005).

[51] G. Y. Guo, S. Murakami, T.-W. Chen, and N. Nagaosa, Intrinsic spin Hall effect in platinum: First-principles calculations, Phys. Rev. Lett. **100**, 096401 (2008).

[52] J. Qiao, J. Zhou, Z. Yuan, and W. Zhao, Calculation of intrinsic spin Hall conductivity by Wannier interpolation, Phys. Rev. B **98**, 214402 (2018).

[53] S. Steiner, S. Khmelevskyi, M. Marsmann, and G. Kresse, Calculation of the magnetic anisotropy with projected-augmented-wave methodology and the case study of disordered $Fe_{1-x}Co_x$ alloys, Phys. Rev. B **93**, 224425 (2016).

[54] Y. Yao, L. Kleinman, A. H. MacDonald, J. Sinova, T. Jungwirth, D.-s. Wang, E. Wang, and Q. Niu, First principles calculation of anomalous Hall conductivity in ferromagnetic bcc Fe, Phys. Rev. Lett. **92**, 037204 (2004).

[55] S. S. Tsirkin, High performance Wannier interpolation of berry curvature and related quantities with WannierBerri code, npj Comput. Mater. **7**, 33 (2021).

[56] D. Destraz, L. Das, S. S. Tsirkin, Y. Xu, T. Neupert, J. Chang, A. Schilling, A. G. Grushin, J. Kohlbrecher, L. Keller, P. Puphal, E. Pomjakushina, and J. S. White, Magnetism and anomalous transport in the Weyl semimetal PrAlGe: Possible route to axial gauge fields, npj Quantum Mater. **5**, 5 (2020).

[57] R. F. Estefania German and A. W. Mombrú, A DFT + U study on structural, electronic, vibrational and thermodynamic properties of TiO_2 polymorphs and hydrogen titanate: Tuning the Hubbard U-term, J. Phys. Commun. **1**, 055006 (2017).

[58] L. Fu and C. L. Kane, Time reversal polarization and a Z_2 adiabatic spin pump, Phys. Rev. B **74**, 195312 (2006).

[59] L. Fu and C. L. Kane, Topological insulators with inversion symmetry, Phys. Rev. B **76**, 045302 (2007).

[60] C. L. Kane and E. J. Mele, Z 2 topological order and the quantum spin Hall effect, Phys. Rev. Lett. **95**, 146802 (2005).

[61] C. Fang, M. J. Gilbert, and B. A. Bernevig, Bulk topological invariants in noninteracting point group symmetric insulators, Phys. Rev. B **86**, 115112 (2012).

[62] A. A. Soluyanov and D. Vanderbilt, Computing topological invariants without inversion symmetry, Phys. Rev. B **83**, 235401 (2011).

[63] R. Yu, X. L. Qi, A. Bernevig, Z. Fang, and X. Dai, Equivalent expression of Z_2 topological invariant for band insulators using the non-abelian berry connection, Phys. Rev. B **84**, 075119 (2011).

[64] Z. Zhu, Y. Cheng, and U. Schwingenschlögl, Band inversion mechanism in topological insulators: A guideline for materials design, Phys. Rev. B **85**, 235401 (2012).

[65] J. Cano, B. Bradlyn, Z. Wang, L. Elcoro, M. G. Vergniory, C. Felser, M. I. Aroyo, and B. A. Bernevig, Building blocks of topological quantum chemistry: Elementary band representations, Phys. Rev. B **97**, 035139 (2018).

[66] M. G. Vergniory, L. Elcoro, Z. Wang, J. Cano, C. Felser, M. I. Aroyo, B. A. Bernevig, and B. Bradlyn, Graph theory data for topological quantum chemistry, Phys. Rev. E **96**, 023310 (2017).

[67] B. Bradlyn, L. Elcoro, J. Cano, M. G. Vergniory, Z. Wang, C. Felser, M. I. Aroyo, and B. A. Bernevig, Topological quantum chemistry, Nature (London) **547**, 298 (2017).

[68] J. Cano, B. Bradlyn, Z. Wang, L. Elcoro, M. G. Vergniory, C. Felser, M. I. Aroyo, and B. A. Bernevig, Topology of disconnected elementary band representations, Phys. Rev. Lett. **120**, 266401 (2018).

[69] Z. Song, T. Zhang, Z. Fang, and C. Fang, Quantitative mappings between symmetry and topology in solids, Nat. Commun. **9**, 3530 (2018).

[70] H. C. Po, A. Vishwanath, and H. Watanabe, Symmetry-based indicators of band topology in the 230 space groups, Nat. Commun. **8**, 50 (2017).

[71] J. Kruthoff, J. De Boer, J. Van Wezel, C. L. Kane, and R.-J. Slager, Topological classification of crystalline insulators through band structure combinatorics, Phys. Rev. X **7**, 041069 (2017).

[72] Y. Du, F. Tang, D. Wang, L. Sheng, E.-j. Kan, C.-G. Duan, S. Y. Savrasov, and X. Wan, CaTe: A new topological node-line and Dirac semimetal, npj Quantum Mater. **2**, 3 (2017).

[73] Y. Kim, B. J. Wieder, C. L. Kane, and A. M. Rappe, Dirac line nodes in inversion-symmetric crystals, Phys. Rev. Lett. **115**, 036806 (2015).

[74] Q. Xu, R. Yu, Z. Fang, X. Dai, and H. Weng, Topological nodal line semimetals in the CaP_3 family of materials, Phys. Rev. B **95**, 045136 (2017).

[75] J. Zhao, R. Yu, H. Weng, and Z. Fang, Topological node-line semimetal in compressed black phosphorus, Phys. Rev. B **94**, 195104 (2016).

[76] L. S. Xie, L. M. Schoop, E. M. Seibel, Q. D. Gibson, W. Xie, and R. J. Cava, A new form of Ca_3P_2 with a ring of Dirac nodes, APL Mater. **3**, 083602 (2015).

[77] A. Yamakage, Y. Yamakawa, Y. Tanaka, and Y. Okamoto, Line-node Dirac semimetal and topological insulating phase in noncentrosymmetric pnictides CaAg X (X = P, As), J. Phys. Soc. Jpn. **85**, 013708 (2016).

[78] S. Ryu and Y. Hatsugai, Topological origin of zero-energy edge states in particle-hole symmetric systems, Phys. Rev. Lett. **89**, 077002 (2002).

[79] T. Fukui and Y. Hatsugai, Quantum spin Hall effect in three dimensional materials: Lattice computation of Z_2 topological invariants and its application to Bi and Sb, J. Phys. Soc. Jpn. **76**, 053702 (2007).

[80] W. Feng, J. Wen, J. Zhou, D. Xiao, and Y. Yao, First-principles calculation of topological invariants within the FP-LAPW formalism, Comput. Phys. Commun. **183**, 1849 (2012).

[81] N. Marzari, A. A. Mostofi, J. R. Yates, I. Souza, and D. Vanderbilt, Wannier90: Maximally localized Wannier functions: Theory and applications, Rev. Mod. Phys. **84**, 1419 (2012).

[82] M. Seemann, D. Ködderitzsch, S. Wimmer, and H. Ebert, Symmetry-imposed shape of linear response tensors, Phys. Rev. B **92**, 155138 (2015).

[83] W. H. Kleiner, Space-time symmetry of transport coefficients, Phys. Rev. **142**, 318 (1966).

[84] Y. Sun, Y. Zhang, C.-X. Liu, C. Felser, and B. Yan, Dirac nodal lines and induced spin Hall effect in metallic rutile oxides, Phys. Rev. B **95**, 235104 (2017).

[85] S. Bhowal and S. Satpathy, Dirac nodal lines and large spin Hall effect in the 6H-perovskite iridate $Ba_3TiIr_2O_9$, Phys. Rev. B **100**, 115101 (2019).

[86] J. Zhou, J. Qiao, A. Bournel, and W. Zhao, Intrinsic spin Hall conductivity of $MoTe_2$ and WTe_2 semimetals, Phys. Rev. B **99**, 060408 (2019).

[87] S. Minami, F. Ishii, M. Hirayama, T. Nomoto, T. Koretsune, and R. Arita, Enhancement of the transverse thermoelectric conductivity originating from stationary points in nodal lines, Phys. Rev. B **102**, 205128 (2020).

[88] A. Sakai, S. Minami, T. Koretsune, T. Chen, T. Higo, Y. Wang, T. Nomoto, M. Hirayama, S. Miwa, D. Nishio-Hamane, F. Ishii, R. Arita, and S. Nakatsuji, Iron-based binary ferromagnets for transverse thermoelectric conversion, Nature (London) **581**, 53 (2020).

[89] M. de Jong, W. Chen, T. Angsten, A. Jain, R. Notestine, A. Gamst, M. Sluiter, C. Krishna Ande, S. Van Der Zwaag, J. J. Plata, C. Toher, S. Curtarolo, G. Ceder, K. A. Persson, and M. Asta, Charting the complete elastic properties of inorganic crystalline compounds, Sci. Data **2**, 150009 (2015).

[90] H. Kleinke and H. F. Franzen, Synthesis, crystal structure, and properties of HfM'P (M' = Fe, Co, Ni) in comparison to ZrNiP, Z. Anorg. Allg. Chem. **622**, 1893 (1996).

[91] E. Ganglberger, H. Nowotny, and F. Benesovsky, Neue e-phasen, Monatsh. Chem. **98**, 95 (1967).

[92] G. A. Landrum, R. Hoffmann, J. Evers, and H. Boysen, The tinisi family of compounds: Structure and bonding, Inorg. Chem. **37**, 5754 (1998).

[93] C. B. Shoemaker and D. P. Shoemaker, A ternary alloy with PbCl$_2$-type structure: TiNiSi(E), Acta Crystallogr. **18**, 900 (1965).

[94] N. Chaichit, P. Chalugune, S. Rukvichai, P. Choosang, V. Kaewchansilp, C.-O. Pontchour, P. Phavananta, S. Pramatus, B. N. Cyvin, and S. J. Cyvin, Crystal structure refinements of ZrCoP, NbCoP, NbNiP and TaFeP, Acta Chem. Scand. **32a**, 309 (1978).